

Tailoring the defect ionization energy to activate the near-infrared photocatalytic activity of poly(heptazine imide)

Guoqiang Zhang^{a,b,1}, Xiaojun Zhang^{a,1}, Yangsen Xu^c, Peixin Zhang^a, Yongliang Li^a, Chuanxin He^a, Hongwei Mi^{a,*}

^a College of Chemistry and Environmental Engineering, Shenzhen University, Shenzhen, Guangdong 518060, China

^b School of Physical Sciences, Great Bay University, Dongguan, Guangdong 523000, China

^c Institute of Information Technology, Shenzhen Institute of Information Technology, Shenzhen, Guangdong 518172, China

ARTICLE INFO

Keywords:

Poly(heptazine imide)
Defect ionization energy
Defect traps
Near-infrared photoactivity
Non-radiative recombination

ABSTRACT

The role of defects in photocatalysis is rarely investigated more intuitively from the perspective of defect ionization energy (DIE), although it is the most important parameter for evaluating the depth of defect traps. Here, the crystalline poly(heptazine imide) (PHI) is adopted as an illustrative example to optimize the DIE and charge separation by regulating the carbon doping contents, ultimately activating the near-infrared photocatalytic activity. Shallow defect traps induced by doping (DIE < 25 meV) facilitate charge separation by releasing shallowly trapped carriers. In contrast, deep defect traps (DIE > 25 meV) act as non-radiative recombination centers, causing carrier quenching. More importantly, the non-radiative recombination rate in PHI is 1–2 orders of magnitude faster than the radiative recombination rate, so suppressing non-radiative recombination is more important for improving charge separation efficiency. Our work elucidates the role of defects in photocatalysis more intuitively from the perspective of DIE, and establishes a discernible relationship between DIE and photocatalytic activity.

1. Introduction

The conversion efficiency from solar to hydrogen needs to reach 10 % to have industrial application value [1,2]. Photocatalysts are required to have a wide spectral response, preferably utilizing near-infrared (NIR) light that accounts for 50 % of the solar energy [3–5]. In comparison to amorphous melon-based polymeric carbon nitride (CN), poly(heptazine imide) (PHI) exhibits superior photocatalytic efficiency due to its highly crystalline structure [6–10]. As a typical *n*-type semiconductor, majority carriers in PHI are electrons. Consequently, constructing shallow trapping sites for electrons becomes particularly important for improving charge separation efficiency and photocatalytic activity. Importantly, these shallow trapping sites, unlike deep trapping sites, do not cause the quenching of photogenerated electrons.

The significance of defects in photocatalysis has been widely recognized [11,12]. Introducing a certain concentration of defects can effectively narrow the band gap of semiconductors and expand light

absorption [13]. More importantly, defects serve as trapping sites for photogenerated electrons/holes, thereby suppressing the direct recombination of photogenerated carriers. However, the deep defect traps can induce non-radiative recombination through the Shockley-Read-Hall mechanism, causing carrier loss and reducing photocatalytic activity [14]. The defect ionization energy (DIE) represents the energy required for valence electrons in defects to become carriers, which is the most important parameter for evaluating the depth of defect traps [15–17]. When it is less than the thermal disturbance energy (~25 meV at room temperature), the defect traps are more likely to release the shallow-trapped electrons/holes. Conversely, the DIE, which is much larger than the thermal disturbance energy, indicates the quenching of carriers. However, the role of defects in photocatalysis is rarely investigated more intuitively from the perspective of DIE, although it is the most important parameter for evaluating the depth of defect traps.

A carbon doping strategy with one stone and two birds has been proposed, which optimizes light absorption and charge separation to activate the NIR photocatalytic activity of PHI. The introduction of 2p

* Corresponding author.

E-mail address: milia807@szu.edu.cn (H. Mi).

¹ These authors contributed equally to this work.

orbital of the doped carbon contributes to the valence band (VB) and narrows the band gap by raising the VB position. In addition, the differences in atomic radius and electronic structure between carbon and nitrogen inevitably induce vacancies and cyano defects. These defects directionally and selectively capture photogenerated electrons, thus preventing the direct recombination of carriers. The optimized DIE is calculated as 15.1 meV, which is close to the shallow acceptor ionization energy (16 meV) in conventional indium-doped silicon semiconductor. Importantly, this value is far less than the thermal disturbance energy, indicating that shallow trapped carriers can be easily released. Our work elucidates the role of defects in photocatalysis more intuitively from the perspective of DIE, and establishes the relationship between DIE and photocatalytic activity.

2. Experimental section

2.1. Chemicals and materials

Urea (99.0 %), KCl (AR, 99.5%), malonic acid (98 %), $\text{H}_2\text{PtCl}_6 \cdot \text{H}_2\text{O}$ (AR, $\text{Pt} \geq 37.5\%$) and triethanolamine (TEOA, AR, 98.0 %) were purchased from Aladdin Reagent Company.

2.2. Preparation of KCN and MKCN

The 10 g of urea and 5 g of KCl were mixed in a 20 mL of the crucible with a cover (sealed with tin foil), and then heated to 600 °C at a rate of 2 °C/min for 3 h in the air. The obtained products were cooled to room temperature, washed with a large amount of water and dried under vacuum at 60 °C for 10 h to obtain KCN. The preparation of MKCN is similar to that of KCN, except for the addition of malonic acid (MA).

According to the different amounts of MA added (x g), the final products were named MKCN- x ($x = 0.3, 0.5, 0.7, 1, 2$). The yield of KCN and MKCN is approximately 10 %.

3. Results and discussion

3.1. Calculation of electronic structures

The electronic structures were investigated by calculating the frontier orbital distributions, energy band structures and density of states (DOS) through the plane-wave technique implemented in the Vienna Ab-initio Simulation Package. The optimized PHI and carbon doped PHI were adopted as structural models [5,18]. The differences in atomic radius and electronic structure between carbon and nitrogen inevitably induce vacancies and cyano defects, so carbon doped PHI with defect was also investigated. The calculated distributions of the highest occupied molecular orbital (HOMO) and lowest unoccupied molecular orbital (LUMO) are shown in Fig. 1a-c. Compared to the relatively uniform distribution in PHI, the HOMO is localized in the three heptazine rings near the doped carbon in carbon-doped PHI, while the LUMO is mainly distributed in the other three heptazine rings far away from the doped carbon. Such spatial separation of HOMO and LUMO facilitates the rapid separation of electrons and holes.

The energy band structures and DOS in Fig. 1d-f indicates that the valence-band maximum (VBM) is contributed by the N state, while the conduction-band minimum (CBM) is composed of N and C hybrid states [5,18]. After carbon doping, the band gap narrows from 2.03 eV of PHI to 1.91 eV. As can be seen from the inset in Fig. 1e, it is the 2p orbitals of doped carbon contribute to the VBM, raising the VB position, while the orbitals of doped carbon do not contribute to the CBM. In addition,

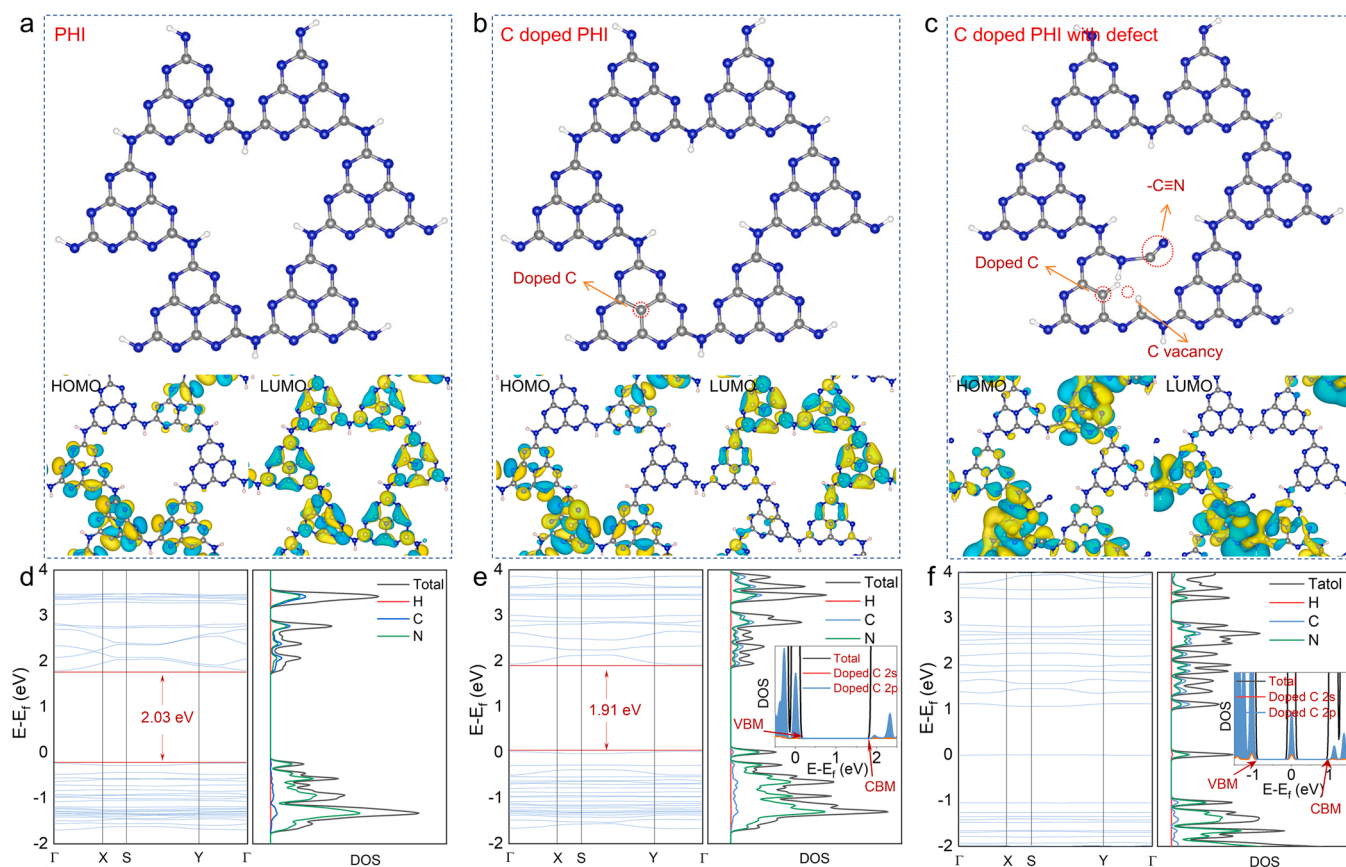


Fig. 1. The optimized structures, and HOMO and LUMO distributions of PHI (a), carbon doped PHI (b), and carbon doped PHI with defect (c), respectively. (d-f) are the corresponding calculated energy band structures and DOS. Insets are DOS contributed by the doped carbon. The atoms of C, N and H are grey, dark blue and white in color, respectively.

carbon doping introduces vacancies and cyano defects, resulting in the generation of intermediate energy levels below CB, as revealed in Fig. 1f. It can be expected that as the carbon doping content increases, the band gap becomes narrower, and the more introduced defects will gradually deepen the intermediate energy levels.

As a typical *n*-type semiconductor, electrons are the majority carriers in PHI, so constructing shallow electron trapping sites is particularly important for improving charge separation efficiency and photocatalytic activity. Considering that vacancies and cyano defects are mainly electron trapping sites, the charge separation efficiency can be optimized by adjusting the depth of defect traps. Specifically, shallow defect traps cause shallow trapping of photogenerated electrons, while deep traps lead to quenching of carriers. In addition, electronic transitions between the raised VB and the introduced intermediate energy levels may result in NIR light absorption. Therefore, the optimization of light absorption and charge separation can be achieved by adjusting the amount of carbon doping, thereby activating NIR photocatalytic activity.

3.2. Preparation and morphology characterization

Inspired by theoretical calculation, a series of PHI samples with the regulated carbon doping were prepared. The activation of NIR photocatalytic activity is expected by optimizing light absorption and charge separation. KCl, as a solid-salt template, can guide the ordered growth of PHI in the confined space among KCl crystals, thereby forming a highly crystalline PHI [4,19–21]. KCN was prepared by thermal polymerization using urea precursors and KCl solid-salt templates. The preparation of MKCN is similar to that of KCN, except for the addition of MA. The synthesis process of MKCN is shown in Fig. 2. Urea undergoes a melting process between 150 and 180 °C, uniformly dissolving MA and KCl. Subsequently, at higher temperatures (greater than 200 °C), urea gradually polymerized into isocyanate, biuret, cyanuric acid, melamine, and melem[22], and precipitates KCl as a hard template. All polymerization processes are conducive to the doping of MA into the heptazine ring through Schiff base polycondensation [23], ultimately synthesizing carbon doped PHI.

The morphology of samples was characterized using field emission scanning electron microscopy (FE-SEM). The KCN, MKCN-0.3 and MKCN-0.7 exhibit nanoparticle morphology with a size of 100–300 nm (Fig. 3a–c), while MKCN-2 shows an amorphous feature (Fig. 3d). In high-resolution transmission electron microscope (HR-TEM, insets in Fig. 3e) images, the clear lattice fringes with a spacing of 1.12 and 0.89 nm can be observed, corresponding to the (100) and (110) crystal planes of PHI structure, respectively. In addition, the diffraction points in the Fast Fourier Transform (FFT, insets in Fig. 3f) pattern further confirm the lattice spacings of 1.12 and 0.89 nm.

High angle annular dark field TEM (HAADF-TEM) coupled with energy dispersive X-ray is adopted to investigate the elemental distributions. As shown in Fig. 3h–k, the elements of C, N, O and K exhibit

uniform distribution across the entire region, indicating a relatively homogeneous incorporation of carbon doping. The urea precursor itself contains oxygen, and PHI is prepared in an air atmosphere, so some oxygen elements may be doped into the PHI structure. According to previous reports [6], potassium element originates from potassium ions embedded in the PHI structure.

3.3. Structural characterization

The X-ray diffraction (XRD) patterns are shown in Fig. 4a. The three diffraction peaks at 7.9°, 9.9° and 28.1° are identified as the (100), (110) and (002) crystal planes of PHI structure [6–10]. All KCN and MKCN samples maintain typical PHI structures. As the amount of MA added increases, the diffraction peak gradually weakens and the main peak shifts to a smaller angle. This is because carbon doping destroys the PHI structure and produces some defects, resulting in the decreased crystallinity and larger interlayer spacing. The Raman spectra is shown in Fig. 4b. The signals from 400 to 800 cm⁻¹ can be assigned to the in-plane stretching vibration mode of heptazine ring, while the peaks in the range of 900–1700 cm⁻¹ correspond to the typically stretching vibration of the C–N [24]. From KCN to MKCN-2, it is evident that the signal intensity gradually decreases, indicating a gradual decrease in crystallinity.

Fourier transform infrared (FTIR, Fig. 4c) spectra are adopted to characterize the characteristic structures. The fingerprint signals at 1100–1700 cm⁻¹ correspond to the stretching and bending vibrations of aromatic heterocycle [25,26], while the peak at 2180 cm⁻¹ belongs to the stretching vibration of cyano group (C≡N). Besides, the signal at 810 cm⁻¹ could be assigned to the out of plane bending vibration of heptazine rings, the signal at 995 cm⁻¹ belong to the symmetric and asymmetric vibrations of NC₂ bonds [27,28]. The cyano signal gradually increases, while the heptazine peak weakens. This is because carbon doping disrupts the heptazine structure, resulting in the formation of cyano defects.

The solid-state cross polarization/magic angle spinning (CP/MAS) ¹³C nuclear magnetic resonance (NMR) are conducted to analyze possible structures and skeletons. As shown in Fig. 4d, the C₁, C₂ and C₃ signals at 172.0, 165.8 and 176.9 ppm correspond to the C atoms in CN₂–(NH_x), C–N₃ and CN₂–N⁺, respectively, confirming the heptazine-based skeleton [29,30]. Elemental analysis shows that the C/N molar ratio in KCN is 0.708, which is very close to the theoretical value of 0.706 for the PHI structure (C₁₂N₁₇H₃). With the addition of MA, the C/N molar ratio increases to 0.724 of MKCN-0.3, 0.752 of MKCN-0.7, and 0.883 of MKCN-2. The K contents in KCN and MKCN samples were tested using inductively coupled plasma-optical emission spectroscopy (ICP-OES, inset of Fig. 4e), ranging from 11.3 wt% to 12.9 wt%.

Above characterizations, including XRD, Raman, FTIR NMR and elemental analysis, have confirmed that carbon doping still maintains the typical PHI structures. Simultaneously, the destruction of heptazine

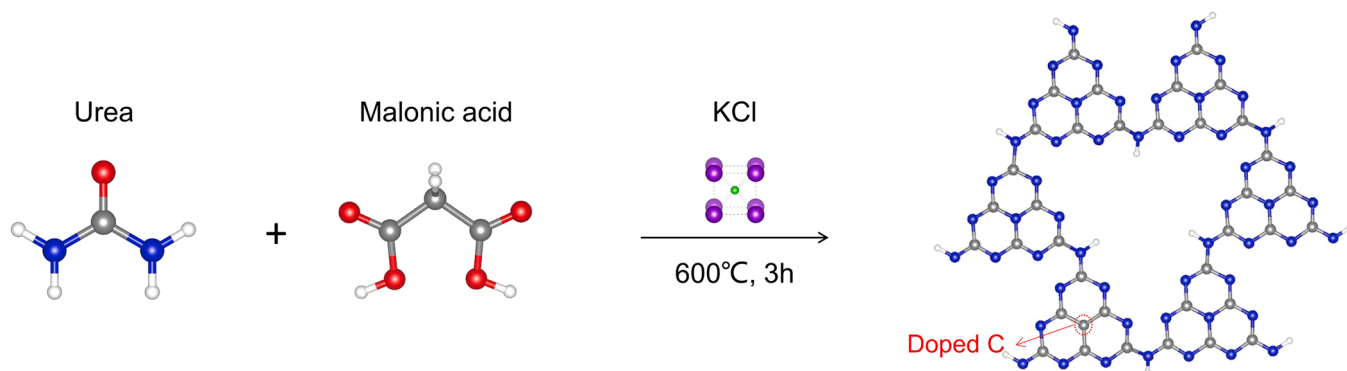


Fig. 2. Synthesis process of MKCN-*x* (*x* = 0.3, 0.5, 0.7, 1.0, 2.0). The atoms of C, N, O, H, K and Cl are in grey, dark blue, red, white, purple and green, respectively.

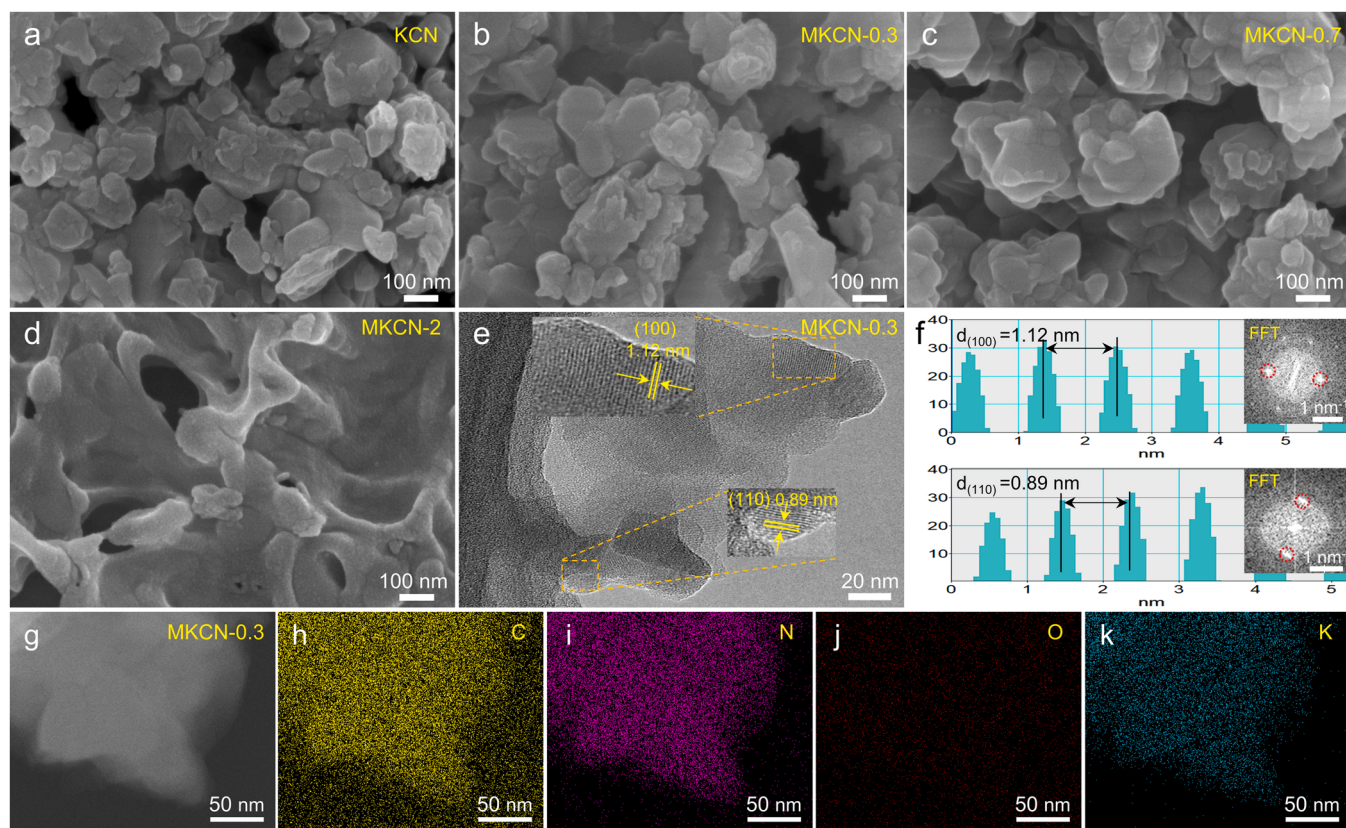


Fig. 3. FE-SEM images of KCN (a), MKCN-0.3 (b), MKCN-0.7 (c) and MKCN-2 (d). HR-TEM images (e), the lattice fringes and FFT patterns (f), HAADF-TEM image (g) and the corresponding elemental mappings (h-k) of MKCN-0.3.

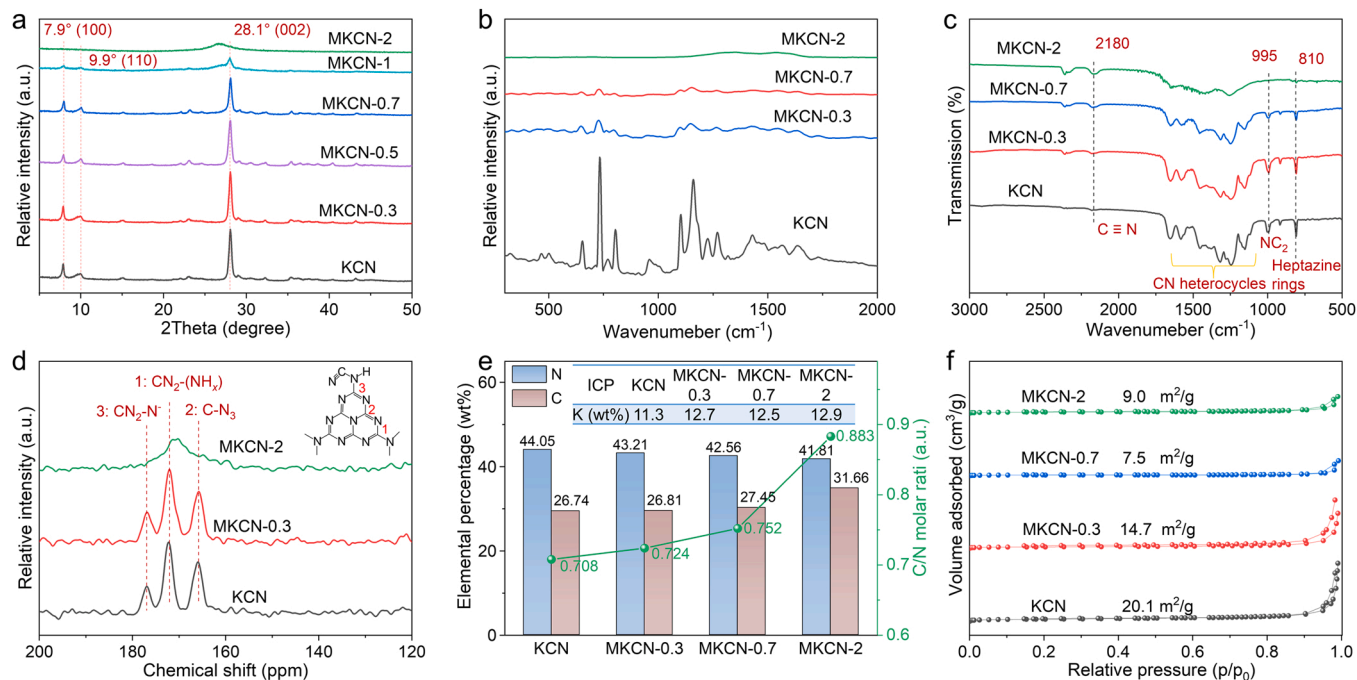


Fig. 4. XRD patterns (a), Raman spectra (b), FTIR spectra (c), ¹³C NMR spectra (d), C/N molar ratio (e) and K contents (inset), and N₂ adsorption-desorption isotherms (f).

structure leads to the formation of vacancies and cyano defects. Thermogravimetric analysis (Figure S1) demonstrates that KCN and MKCN have similar thermal stability, both of them losing water before 200 °C

and decomposing violently after 600 °C. The N₂ isothermal adsorption-desorption curves were employed to characterize the specific surface area of samples. As shown in Fig. 4f, all samples present II-type

adsorption-desorption curves with H3-type hysteresis loops, indicating the mesoporous and macroporous structures. The BET specific surface areas were determined to be 20.1, 14.7, 7.5 and 9.0 m²/g for KCN, MKCN-0.3, MKCN-0.7 and MKCN-2, respectively. The specific surface area is related to the size and compactness of the particles. As can be seen in Fig. 3, the particles from KCN, MKCN-0.3 to MKCN-0.7 are gradually packed tightly, which may lead to a decrease in specific surface area. MKCN-2 presents a typical amorphous morphology, which results in an increase in the specific surface area.

3.4. XPS analysis

X-ray photoelectron spectra (XPS) are performed to characterize the chemical structures. XPS survey spectra (Fig. 5a) reveal the existence of C, N, O, Cl and K elements in both KCN and MKCN samples. The C 1s high-resolution XPS can be fitted into three peaks at 287.7, 286.5, and 284.8 eV (Fig. 5b), belonging to C atoms in aromatic N=C=N units, C≡N and C-C, respectively [31,32]. The area ratio of C-C gradually increases from KCN (14.3 %) to MKCN-0.3 (16.5 %), MKCN-0.7 (25.4 %), and MKCN-2 (34.3 %). The area ratio of C≡N also shows enhancement as the increase of doped carbon. In addition, the carbon doping increases the electron density of the overall structure, leading to the decreased binding energy of C atoms in aromatic N-C=N [33].

Besides, the N 1s XPS exhibits three contributions, located at 398.8, 400.3 and 401.2 eV (Fig. 5c), which could be attributed to N atoms in C-N=C, N-(C)₃ and bridging-NH_x, respectively [34,35]. The area ratio of N-(C)₃ gradually decreases from KCN to MKCN-2, possibly due to the destruction of heptazine structure caused by carbon doping [5]. In Fig. 5d, the K 2p_{1/2} and K 2p_{3/2} peaks with a spin-orbit splitting of 2.8 eV are observed at 295.7 and 292.9 eV, respectively, which can be classified as K⁺ ions. The Cl 2p_{1/2} and Cl 2p_{3/2} peaks at 199.5 and 197.7 eV

(Figure S2) indicate the presence of trace Cl⁻ ions (less than 0.3 at%), possibly from surface adsorption. XPS confirms the successful carbon doping, which destroys the heptazine structure and induces the generation of vacancies and cyano defects.

3.5. Absorption characteristics and intermediate energy levels

Carbon-doped PHI narrows the band gap by raising the VB position. Concurrently, the introduced defects, including vacancies and cyano defects, generate intermediate energy levels below the CB [5]. The ultraviolet-visible-near infrared diffuse reflectance spectra (UV-Vis-NIR DRS, Fig. 6a) were employed to investigate the absorption characteristics of samples. With the increase of carbon doping amount, the absorption gradually expands, showing significant absorption in NIR region (700–900 nm). The colors of the samples deepen, changing from yellow (KCN) to orange yellow (MKCN-0.3), and finally to dark brown (MKCN-2) (insets in Fig. 6a). The Urbach tail energy (E_U) was calculated to investigate the intermediate energy levels below the CB [36]. As shown in inset in Fig. 6a, the band tail states increase from 0.13 to 0.59 eV, and then decrease to 0.56 and 0.53 eV. This is due to the introduction of intermediate energy levels below the CB by vacancies and cyano defects, which enhances the band tail states. With the increase of intermediate energy levels, the CB becomes more and more continuous, resulting in a decrease in E_U value [37].

According to Tauc plots (Fig. 6b), the band gap of KCN is calculated as 2.71 eV, while the MKCN series samples present obvious narrowing with the band gaps of 2.43 (MKCN-0.3), 2.39 (MKCN-0.7) and 2.35 eV (MKCN-2), respectively. In addition, as shown in inset in Fig. 6b, there are intermediate band gaps of 1.76, 1.69 and 1.63 eV, which belong to the electron transition from the VB to the intermediate energy levels. Such a small band gap is sufficient to absorb NIR light and generate NIR

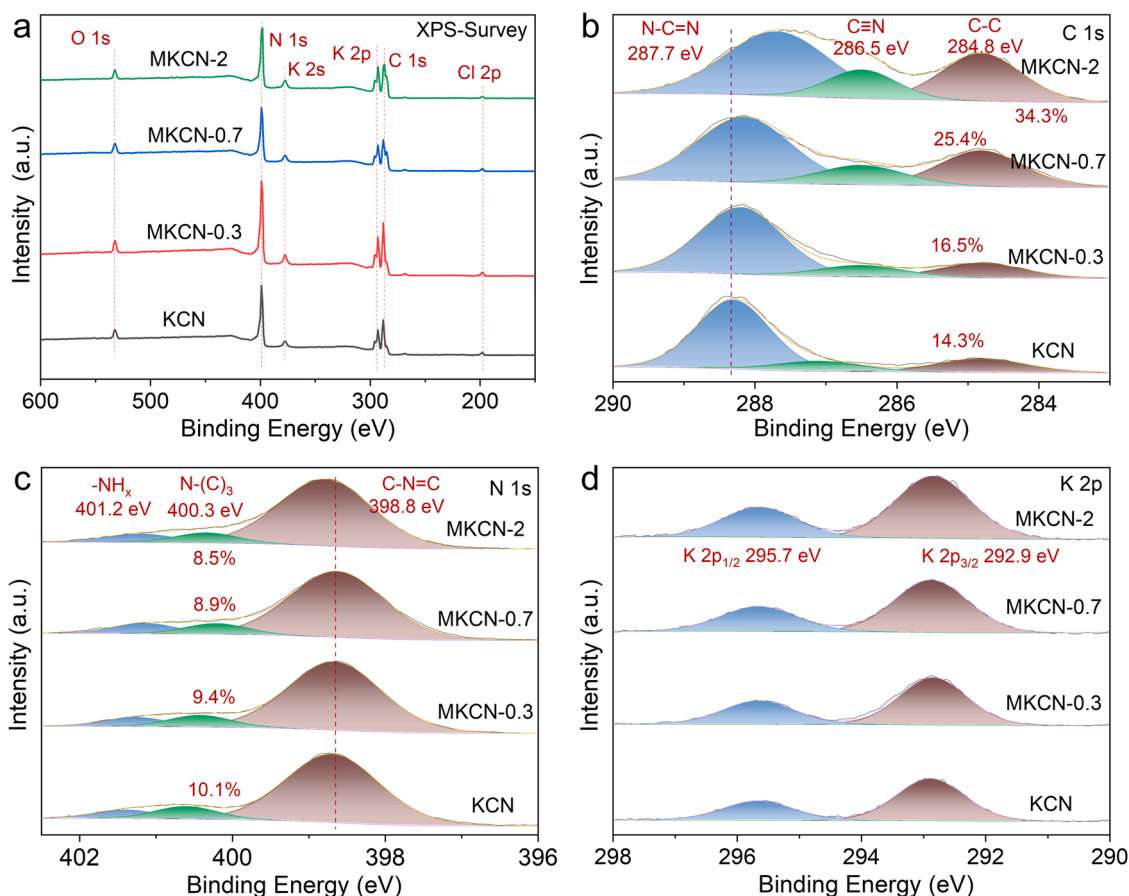


Fig. 5. The XPS survey spectra (a) and high-resolution XPS spectra (b-d).

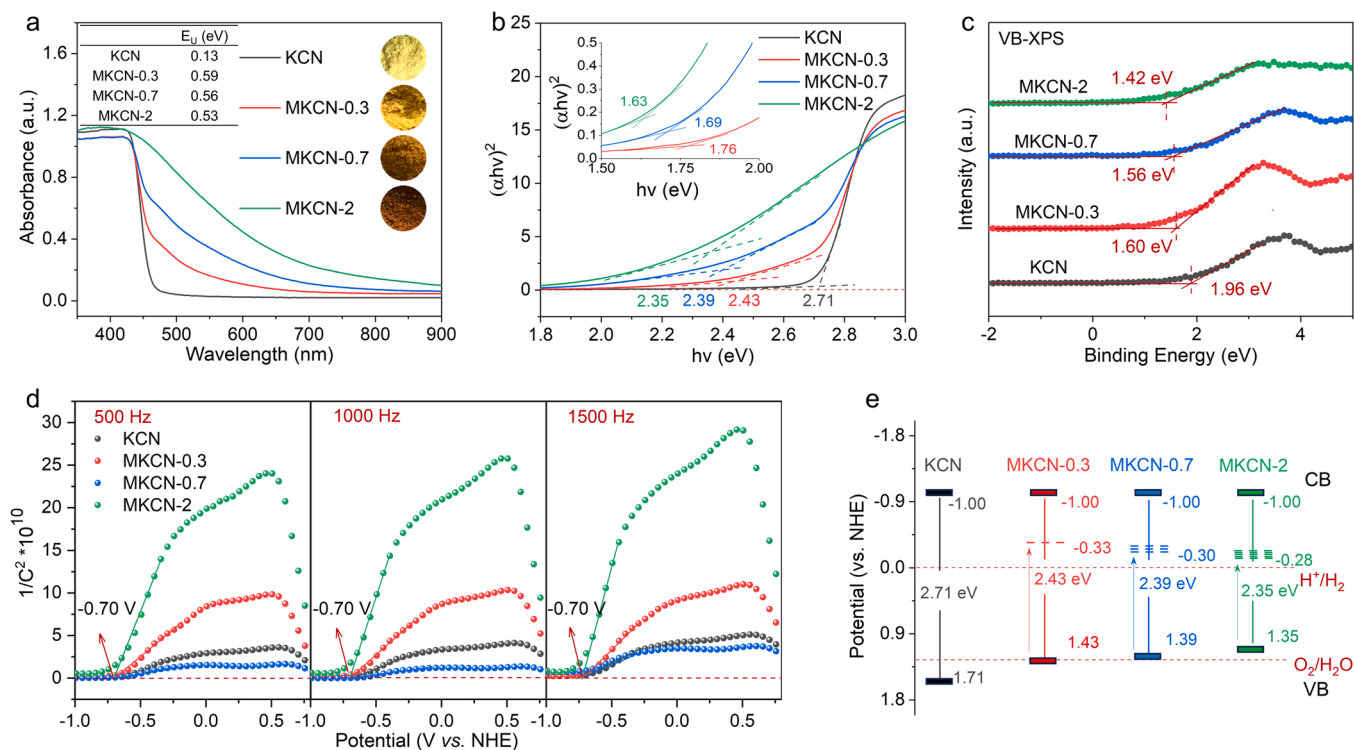


Fig. 6. UV-Vis-NIR DRS (a), the calculated Urbach tail energy (insets) and optical photographs (insets). Tauc plots of transformed Kubelka-Munk function vs. the energy (b), VB-XPS (c), Mott-Schottky plots (d), and energy band structures (e).

photoactivity. The VB-XPS (Fig. 6c) shows that the relative positions of VB in KCN and MKCN samples are 1.96, 1.60, 1.56 and 1.42 eV, respectively, showing a significant rise. These VB positions are not absolute, but relative to the Fermi level of the XPS instrument, and are used only to represent the trend of VB changes. The absolute position of VB is calculated from the band gap and the CB measured by Mott-Schottky. In Mott-Schottky plots (Fig. 6d), both KCN and MKCN samples exhibit positive slope curves of typical *n*-type semiconductors. The flat band potential (E_{fb}) is -0.70 V relative to the normal hydrogen electrode (NHE). Considering that the CB potential relative to E_{fb} is 0.30 V in *n*-type semiconductors, the CB position is -1.00 V vs. NHE.

From the diagram of energy band structures (Fig. 6e), it can be seen that the band gap from KCN to MKCN-2 gradually decreases. This is because the 2p orbitals of doped carbon contribute to the formation of VB, causing VB position to rise. The positions of the intermediate energy level can be calculated from the intermediate band gaps, which were -0.43 , -0.34 and -0.28 V vs. NHE in MKCN-0.3, MKCN-0.7 and MKCN-2, respectively. Clearly, from MKCN-0.3 to MKCN-2, the position of the intermediate levels gradually moves away from CB, confirming the deepened intermediate levels. The increase in defect concentration will enhance the DIE. When it is less than the thermal disturbance energy, the defect traps are more likely to release the shallow-trapped electrons. Conversely, the DIE, which is much larger than the thermal disturbance energy, indicates the quenching of carriers. Therefore, the charge separation efficiency can be optimized by adjusting the defect concentration and trap depth, ultimately activating NIR photocatalytic activity.

3.6. Photocatalytic activity analysis

Regulating the carbon doping content can optimize the NIR light absorption and charge separation efficiency, thereby activating NIR photoactivity. The photocatalytic activity for H_2 evolution was investigated under $420 \text{ nm} < \lambda < 780 \text{ nm}$, $500 \text{ nm} < \lambda < 780 \text{ nm}$ and $700 \text{ nm} < \lambda < 780 \text{ nm}$ irradiations, respectively (Fig. 7a-c). TEOA was used as sacrificial agent and 3 wt% Pt as co-catalyst to produce H_2 . All tests were

controlled at 5°C by recirculating cooling water system.

As shown in Fig. 7a, under $420 \text{ nm} < \lambda < 780 \text{ nm}$ irradiation, the trend of H_2 production rate increases first and then decreases from KCN to MKCN. MKCN-0.3 presents the highest H_2 production rate of $220.8 \mu\text{mol/h}$, which is 2.1 times that of KCN. Similarly, MKCN-0.3 appears the highest activity of $102.6 \mu\text{mol/h}$ under $500 \text{ nm} < \lambda < 780 \text{ nm}$ irradiation, 85.5 times that of KCN (Fig. 7b). In addition, the NIR photoactivity of MKCN samples was activated, while KCN has no NIR photoactivity. MKCN-0.3 exhibits the best activity at $4.0 \mu\text{mol/h}$ (Fig. 7c). The carbon doping causes the narrowing of band gap and the enhancement of NIR light absorption. As the DIE gradually increases and trap deepens, it becomes the non-radiative recombination center of carriers, resulting in a decrease in photocatalytic efficiency.

Solar apparent quantum efficiency (AQE) refers to the ratio of the number of photons utilized for H_2 production under sunlight to the number of incident photons. A xenon lamp equipped with an AM 1.5 G filter was used to measure the Solar AQE. According to the equivalent wavelength of sunlight is 584.3 nm (GB/T 26915–2011), the Solar AQE value of MKCN-0.3 sample is calculated as 0.83% (Fig. 7d). The wavelength-dependent AQE is measured using different monochromatic light irradiations. As shown in Fig. 7e, the change in AQE is consistent with light absorption, indicating the light induced H_2 production. The AQE of MKCN-0.3 at 420 and 500 nm is 13.39% and 2.24% , respectively. Even at 700 nm , its AQE is still 0.11% . The cyclic stability test is shown in Fig. 7f. After eight cycles, the activity is basically not attenuated, indicating the excellent light stability of MKCN-0.3 sample. In addition, in Figure S3 and S4, there are no significant changes in the XRD, XPS and TEM results of the sample before and after photocatalytic cycle, further proving the photostability of MKCN-0.3. Fig. 7g is the comparison of NIR H_2 production activity between MKCN-0.3 and the reported CN photocatalysts. MKCN-0.3 exhibits a NIR photoactivity of $4.0 \mu\text{mol/h}$, which is at a relatively high level among the reported CN photocatalysts [4,18,21,38–45].

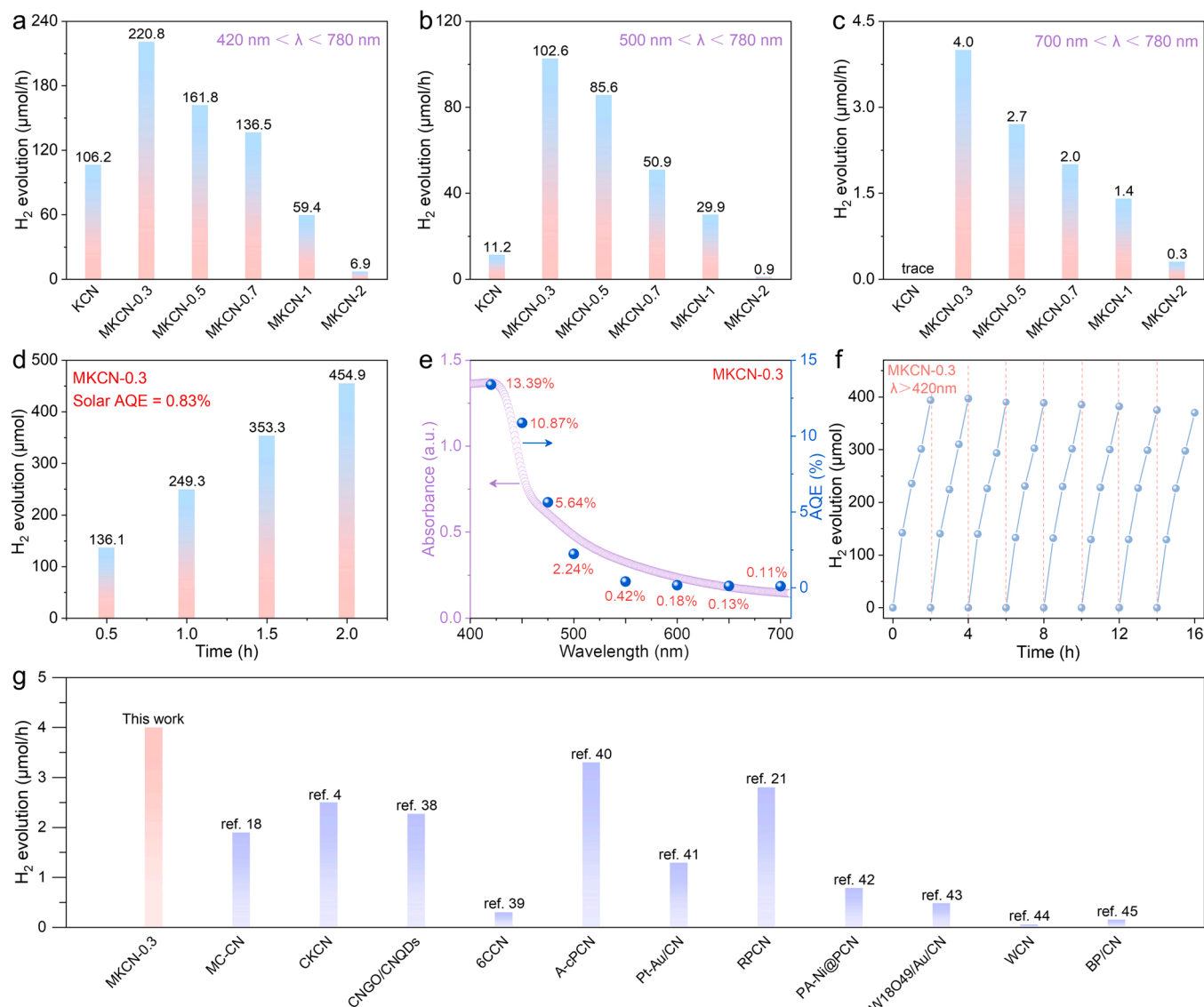


Fig. 7. H₂ evolution under 420 nm < λ < 780 nm (a), 500 nm < λ < 780 nm (b) and 700 nm < λ < 780 nm (c) irradiations, respectively. H₂ production under simulated sunlight (d), wavelength-dependent AQE under monochromatic light irradiations (e), and cyclic H₂ production test (f). (g) is the comparison of NIR H₂ production activity between MKCN-0.3 and the reported CN photocatalysts.

3.7. Carrier transport and separation

The carbon doped PHI introduces vacancies and cyano defects. As shown in Fig. 8a, the defect concentration was quantitatively analyzed through electron paramagnetic resonance (EPR) at 77 K. The number of unpaired electron spins increases from 1.41×10^{16} (KCN) to 2.25×10^{16} (MKCN-0.3), 3.49×10^{16} (MKCN-0.7) and 4.78×10^{16} (MKCN-2) spins/cm³, confirming the gradual increase in defect concentration. The carrier mobility and carrier concentration were characterized using Hall effect measurement system (Fig. 8b). Defects can cause the capture and scattering of carriers, so the carrier mobility gradually decreases with the increase of defects. From KCN to MKCN-2, the carrier concentration first increases and then decreases. MKCN-0.3 has the highest carrier concentration, which can be attributed to the shallow defect traps providing more carriers. As the traps continue to deepen, the carrier concentrations of MKCN-0.7 and MKCN-2 gradually decrease, due to the quenching of carriers caused by deep defect traps.

The wide band gap of samples is difficult to be thermally excited at room temperature, so the carriers are derived from the thermal excitation of defects. DIE is the energy required for valence electrons in defects

to become carriers, which can investigate the depth of defect traps. The DIE can be determined by the formula " $E_I = -k_B T \ln(n/N)$ ", where E_I is the DIE, k_B is the Boltzmann constant, T is temperature, n is the carrier concentration, and N is the defect concentration. The E_I is calculated as 5.0, 15.1, 26.7 and 34.6 meV, showing a significant increase, which indicates a gradual deepening of defect traps. In MKCN-0.3 and MKCN-2 samples, the DIE is much lower and larger than the thermal disturbance energy (~25 meV at room temperature), respectively, corresponding to shallow defect traps promoting charge separation and deep traps leading to carrier quenching.

In steady-state photoluminescence (PL, Fig. 8c), the emission wavelengths of KCN, MKCN-0.3, MKCN-0.7 and MKCN-2 are 461.2, 503.8, 505.0, and 537.2 nm, respectively. The emission wavelengths of MKCN gradually redshift due to the narrowing of the band gap, compared with KCN. The PL intensity shows a gradual decrease, attributed to defects acting as electron traps, which suppress the direct recombination of carriers. In addition, as the defect trap deepens, it acts as a non-radiative recombination center, greatly reducing radiative recombination and PL intensity [46]. Time-resolved photoluminescence (TRPL) spectra were employed to investigate the decay process of

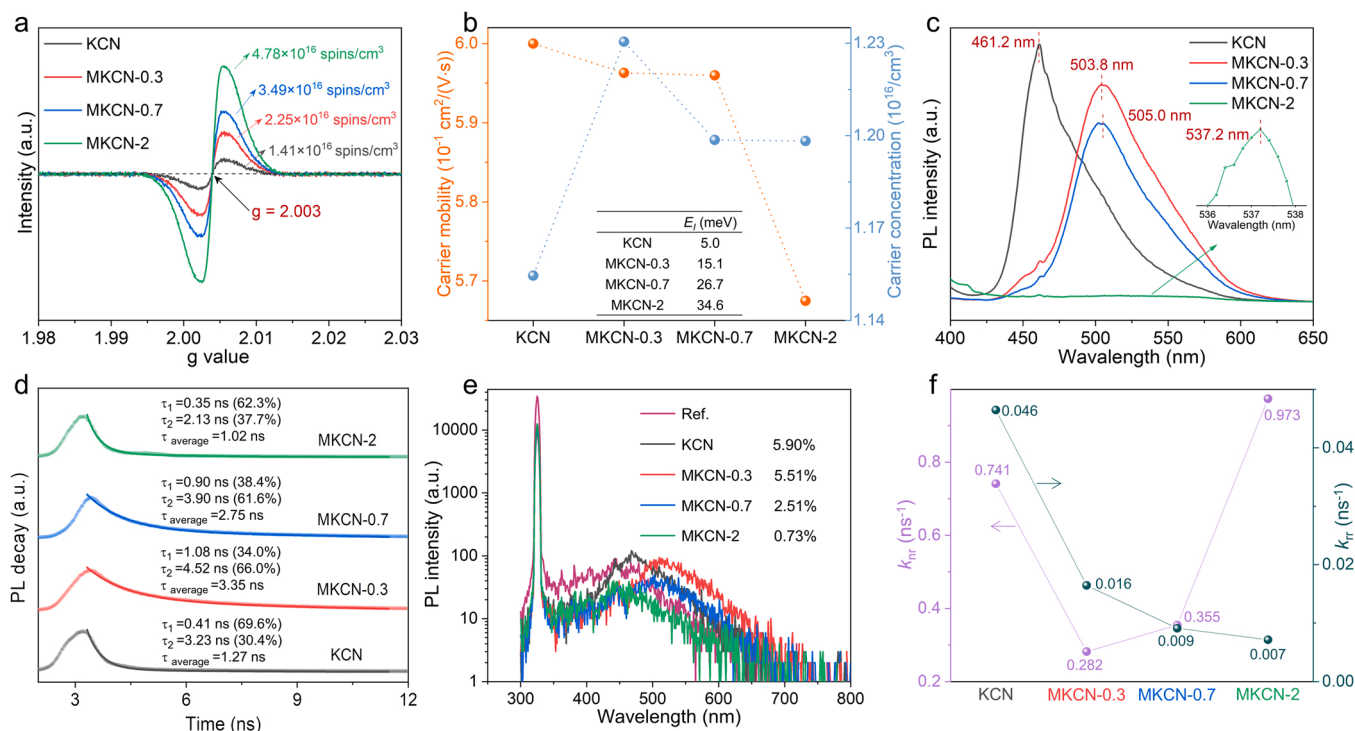


Fig. 8. EPR (a), carrier mobility and carrier concentration in Hall Effect Testing (b), the calculated DIE (inset), steady-state PL (c), TRPL (d), PLQY excited at 325 nm laser (e), and the calculated k_{tr} and k_{nr} .

photogenerated carrier, which can be well fitted as double-exponential functions in Fig. 8d. From KCN to MKCN-2, both τ_1 , τ_2 and τ_{average} increases first and then decreases, which is consistent with the photocatalytic performance. In MKCN-0.3, the shallow defect traps, can release shallowly trapped carriers, resulting in the longest fluorescence lifetime. However, the deep defect traps in MKCN-0.7 and MKCN-2 serve as non-radiative recombination centers, leading to carrier quenching and reduced lifetime.

Photoluminescence quantum yield (PLQY, Fig. 8e) test was performed to further characterize the carrier non-radiative recombination rate (k_{nr}) and radiative-recombination rate (k_{tr}). All samples were excited at 325 nm laser. According to formulas “ $\text{PLQY} = \frac{k_{tr}}{k_{tr} + k_{nr}}$ ” and “ $\tau_{\text{average}} = \frac{1}{k_{tr} + k_{nr}}$ ” [47,48], the k_{nr} and k_{tr} can be calculated. As shown in Fig. 8f, defect traps can capture photogenerated electrons and suppress direct recombination of carriers, resulting in a gradually decreasing k_{tr} . MKCN-0.3 exhibits the minimum k_{nr} , which is an important factor leading to its highest photocatalytic activity. In addition, as the defect trap deepens, it acts as non-radiative recombination centers in MKCN-0.7 and MKCN-2, leading to an increased k_{nr} . More importantly, considering that the k_{nr} in PHI is 1–2 orders of magnitude faster than the k_{tr} , the suppression of non-radiative recombination is more important for improving charge separation efficiency [5].

The photoelectric response of samples was examined by visible-light photocurrent measurement. As shown in Figure S5, no photocurrent signal in dark for all the samples. Under visible-light, MKCN-0.3 exhibit the most stable and stronger photocurrent intensity in each cycle, indicating the efficient charge separation promoted by shallow defect traps. Besides, MKCN-0.3 has the smallest Nyquist radius in electrochemical impedance spectroscopy (EIS, Figure S6), which greatly reduces the resistance of carrier migration. In summary, these characterizations, including Hall, PL, TRPL, PLQY, photocurrent and EIS measurements, confirm that shallow defect traps (DIE < 25 meV) promote charge separation by releasing shallowly trapped carriers, while deep traps (DIE > 25 meV) act as non-radiative recombination centers, causing carrier quenching.

3.8. fs-TA analysis

The ultrafast femtoseconds transient absorption (fs-TA) spectroscopy is performed to illustrate the dynamics of photogenerated carriers [49]. Compared to TRPL, fs-TA can provide carrier information on much shorter timescales, such as picosecond or even femtosecond scales. Both KCN and MKCN samples are excited from the ground state to the excited state at 400 nm pump light. Fig. 9a-h show the fs-TA spectra (430–800 nm) at different probe delays, representing ground state bleaching and excited state absorption signals, respectively. With the extension of probe delays, the TA signal gradually decreases, indicating the reduced active carriers. From KCN to MKCN-2, the signal peak of ground state bleaching gradually shifts red, consistent with the narrowed band gap. In addition, the TA signal first increases and then decreases, which is consistent with the shallow defect traps promoting charge separation and deep traps causing carrier quenching.

The decay dynamics of photogenerated carriers probed at 460/480 nm can be well fitted by a double-exponential function (Fig. 9i-l). The shorter lifetime (< 5 ps) can be attributed to the process of trapping electrons by the defect traps, while the longer lifetime (> 50 ps) belongs to the process of trapping electrons in the defect traps back to the VB [50]. The shallow defect traps in MKCN-0.3 can release shallowly trapped carriers. As the defect traps gradually deepens, the deeply trapped carriers are quenched. Therefore, MKCN-0.3 shows the longest τ_1 , τ_2 and τ_{average} . In addition, the weight of τ_2 increases first and then decreases, which is attributed to the shallow trapping of carriers by shallow defect traps and the quenching of carriers by deep defect traps.

4. Conclusions

A carbon doping strategy with one stone and two birds has been proposed, which optimizes light absorption and charge separation to activate the NIR photocatalytic activity of PHI. Carbon doping narrows the band gap by raising the VB position. In addition, vacancies and cyano defects induced by carbon doping result in the formation of intermediate energy levels below the CB. The electron transitions between

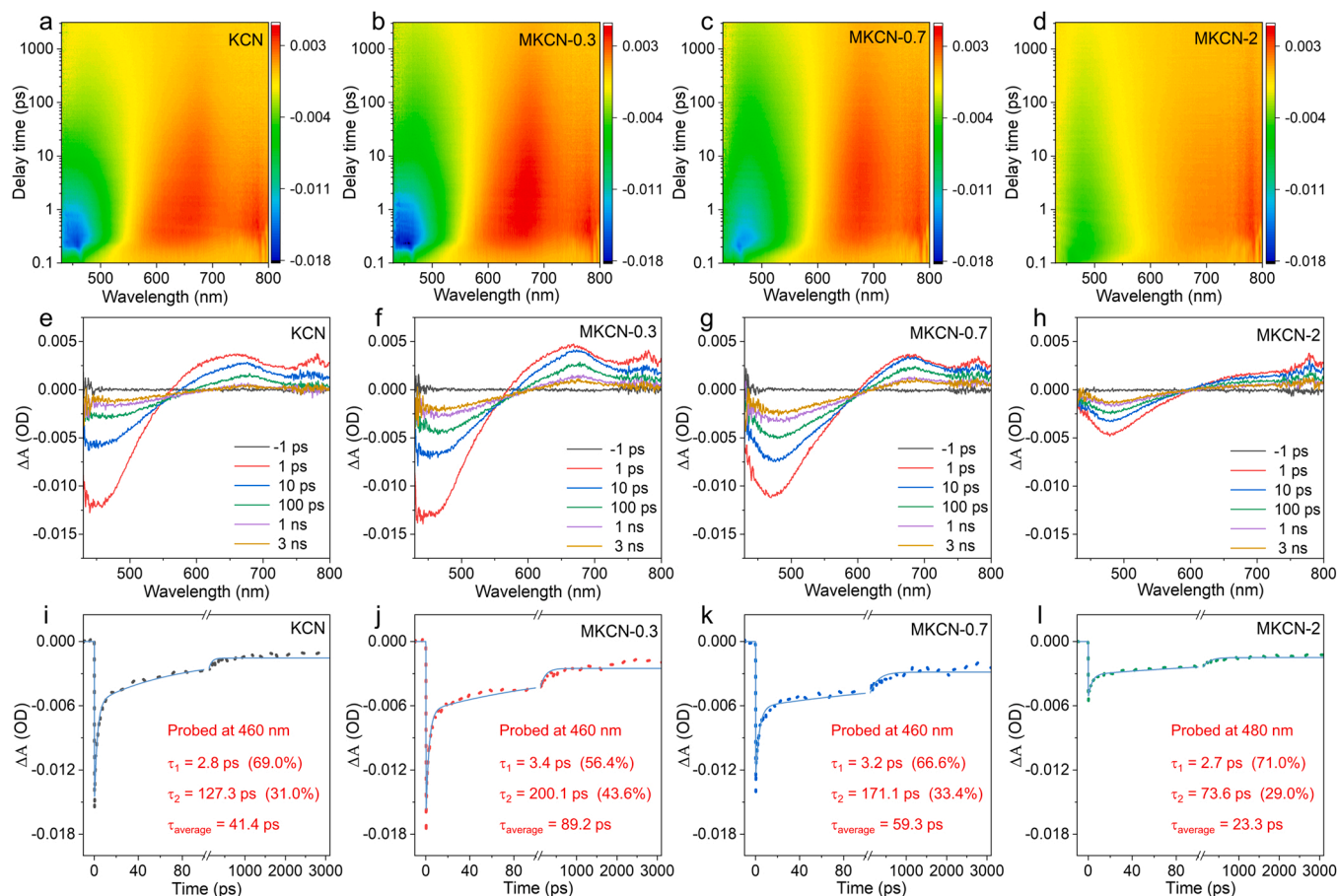


Fig. 9. Time-wavelength-dependent TA color maps (pump at 400 nm) (a-d). Representative TA spectra at different probe delays (e-h). TA decay kinetics probed at 460/480 nm (i-l).

the VB and these intermediate energy levels contribute NIR light absorption. As the carbon doping content improves, the defect concentration increases, leading to the improved DIE value and deepening defect traps. Since the k_{nr} of PHI is 1–2 orders of magnitude faster than the k_{rr} , the suppression of non-radiative recombination is more important for improving charge separation efficiency. Our work provides a more intuitive explanation of the role of defects in photocatalysis from the perspective of DIE, and establishes the relationship between DIE and photocatalytic activity.

CRediT authorship contribution statement

Guoqiang Zhang: Writing – original draft, Project administration, Investigation, Funding acquisition, Data curation, Conceptualization. **Hongwei Mi:** Writing – review & editing, Supervision, Funding acquisition, Conceptualization. **Chuanxin He:** Supervision. **Yongliang Li:** Supervision. **Peixin Zhang:** Supervision, Funding acquisition. **Yangsen Xu:** Writing – review & editing. **Xiaojun Zhang:** Writing – original draft, Project administration, Investigation, Data curation.

Declaration of Competing Interest

The authors declare that they have no known competing financial interests or personal relationships that could have appeared to influence the work reported in this paper.

Data availability

Data will be made available on request.

Acknowledgements

This work was jointly supported by the National Science Foundation of China (22102103), Shenzhen Science and Technology Program (JCYJ20220531102617040) and Talent Introduction Project of Great Bay University (YJKY230013). The Instrumental Analysis Center of Shenzhen University was also gratefully acknowledged.

Appendix A. Supporting information

More TG, XPS, photocurrent and EIS measurements are shown in the supplementary information. Supplementary data associated with this article can be found in the online version at [doi:10.1016/j.apcatb.2024.124200](https://doi.org/10.1016/j.apcatb.2024.124200).

References

- [1] K. Zhang, L. Guo, Metal sulphide semiconductors for photocatalytic hydrogen production, *Catal. Sci. Technol.* 3 (2013) 1672–1690.
- [2] Q. Wang, K. Domen, Particulate photocatalysts for light-driven water splitting: mechanisms, challenges, and design strategies, *Chem. Rev.* 120 (2020) 919–985.
- [3] Y. Yang, H. Tan, B. Cheng, J. Fan, J. Yu, W. Ho, Near-infrared-responsive photocatalysts, *Small Methods* 5 (2021) 2001042.
- [4] G. Zhang, Y. Xu, M. Rauf, J. Zhu, Y. Li, C. He, X. Ren, P. Zhang, H. Mi, Breaking the limitation of elevated coulomb interaction in crystalline carbon nitride for visible and near-infrared light photoactivity, *Adv. Sci.* 9 (2022) 2201677.
- [5] G. Zhang, W. Huang, Y. Xu, Y. Li, C. He, X. Ren, P. Zhang, H. Mi, Suppressing defects-induced non-radiative recombination for activating the near-infrared photoactivity of red polymeric carbon nitride, *Adv. Funct. Mater.* 33 (2023) 2305935.
- [6] H. Schlömer, J. Kröger, G. Savasci, M.W. Terban, S. Bette, I. Moudrakovski, V. Duppel, F. Podjaski, R. Siegel, J. Senker, R.E. Dinnebier, C. Ochsenfeld, B.

- V. Lotsch, Structural Insights Into Poly(heptazine Imides): A Light-storing Carbon Nitride Material for Dark Photocatalysis, *Chem. Mater.* 31 (2019) 7478–7486.
- [7] J. Kröger, A. Jiménez-Solano, G. Savasci, P. Rovó, I. Moudrakovski, K. Küster, H. Schlöberg, H.A. Vignolo-González, V. Duppel, L. Grunenberg, C.B. Dayan, M. Sitti, F. Podjaski, C. Ochsenfeld, B.V. Lotsch, Interfacial engineering for improved photocatalysis in a charge storing 2D carbon nitride: melamine functionalized poly(heptazine imide), *Adv. Energy Mater.* 11 (2021) 2003016.
- [8] F. Guo, B. Hu, C. Yang, J. Zhang, Y. Hou, X. Wang, On-surface polymerization of in-plane highly ordered carbon nitride nanosheets toward photocatalytic mineralization of mercaptan gas, *Adv. Mater.* 33 (2021) 2101466.
- [9] Z. Chen, A. Savateev, S. Pronkin, V. Papaefthimiou, C. Wolff, M.G. Willinger, E. Willinger, D. Neher, M. Antonietti, D. Dontsova, “The Easier the Better” preparation of efficient photocatalysts-metastable poly(heptazine imide) salts, *Adv. Mater.* 29 (2017) 1700555.
- [10] G. Zhang, Y. Xu, J. Zhu, Y. Li, C. He, X. Ren, P. Zhang, H. Mi, Enhanced photocatalytic H₂ production independent of exciton dissociation in crystalline carbon nitride, *Appl. Catal. B-Environ.* 338 (2023) 123049.
- [11] E. Pastor, M. Sachs, S. Selim, J.R. Durrant, A.A. Bakulin, A. Walsh, Electronic defects in metal oxide photocatalysts, *Nat. Rev. Mater.* 7 (2022) 503–521.
- [12] Y.-C. Zhang, N. Afzal, L. Pan, X. Zhang, J.-J. Zou, Structure-activity relationship of defective metal-based photocatalysts for water splitting: experimental and theoretical perspectives, *Adv. Sci.* 6 (2019) 1900053.
- [13] X. Chen, L. Liu, P.Y. Yu, S.S. Mao, Increasing Solar Absorption for Photocatalysis with Black Hydrogenated Titanium Dioxide Nanocrystals, *Science* 331 (2011) 746–750.
- [14] S.R. Cowan, W.L. Leong, N. Banerji, C. Dennler, A.J. Heeger, Identifying a threshold impurity level for organic solar cells: enhanced first-order recombination via well-defined PC84BM traps in organic bulk heterojunction solar cells, *Adv. Funct. Mater.* 21 (2011) 3083–3092.
- [15] K. Nagasaka, S.I. Narita, Effect of impurity interaction upon ionization energy of donor-electrons in germanium, *J. Phys. Soc. Jpn.* 35 (1973) 797–805.
- [16] J.L. Pautrat, Electric field and impurity concentration effects on the ionization energy of impurities. Application to acceptors in ZnTe, *Solid State Electron* 23 (1980) 661–670.
- [17] M. Diarra, Y.-M. Niquet, C. Delerue, G. Allan, Ionization energy of donor and acceptor impurities in semiconductor nanowires: importance of dielectric confinement, *Phys. Rev. B* 75 (2007) 045301.
- [18] B. Zhai, H. Li, G. Gao, Y. Wang, P. Niu, S. Wang, L. Li, A crystalline carbon nitride based near-infrared active photocatalyst, *Adv. Funct. Mater.* 32 (2022) 2207375.
- [19] G.Q. Zhang, Y.S. Xu, D.F. Yan, C.A.X. He, Y.L. Li, X.Z. Ren, P.X. Zhang, H.W. Mi, Construction of K⁺ ion gradient in crystalline carbon nitride to accelerate exciton dissociation and charge separation for visible light H₂ production, *ACS Catal.* 11 (2021) 6995–7005.
- [20] G. Zhang, Y. Xu, C. He, P. Zhang, H. Mi, Oxygen-doped crystalline carbon nitride with greatly extended visible-light-responsive range for photocatalytic H₂ generation, *Appl. Catal. B-Environ.* 283 (2021) 119636.
- [21] Y.S. Xu, M.J. Fan, W.J. Yang, Y.H. Xiao, L.T. Zeng, X. Wu, Q.H. Xu, C.L. Su, Q.J. He, Homogeneous carbon/potassium-incorporation strategy for synthesizing red polymeric carbon nitride capable of near-infrared photocatalytic H₂ production, *Adv. Mater.* 33 (2021) 2101455.
- [22] Y. Zhang, J. Liu, G. Wu, W. Chen, Porous graphitic carbon nitride synthesized via direct polymerization of urea for efficient sunlight-driven photocatalytic hydrogen production, *Nanoscale* 4 (2012) 5300–5303.
- [23] J. Zhang, X. Chen, K. Takanabe, K. Maeda, K. Domen, J.D. Epping, X. Fu, M. Antonietti, X. Wang, Synthesis of a carbon nitride structure for visible-light catalysis by copolymerization, *Angew. Chem. Int. Ed.* 49 (2010) 441–444.
- [24] H. Yang, S. Sun, J. Lyu, Q. Yang, J. Cui, Mechanism insight into triple S-Scheme intermolecular carbon nitride homojunction with robust built-in electric field for highly enhanced photocatalytic hydrogen evolution, *Chem. Eng. J.* 481 (2024) 148297.
- [25] J. Zhang, G. Zhang, X. Chen, S. Lin, L. Möhlmann, G. Dolega, G. Lipner, M. Antonietti, S. Blechert, X. Wang, Co-monomer control of carbon nitride semiconductors to optimize hydrogen evolution with visible light, *Angew. Chem. Int. Ed.* 51 (2012) 3183–3187.
- [26] M. Shalom, S. Inal, C. Fetzkenhauer, D. Neher, M. Antonietti, Improving carbon nitride photocatalysis by supramolecular preorganization of monomers, *J. Am. Chem. Soc.* 135 (2013) 7118–7121.
- [27] A. Savateev, S. Pronkin, J.D. Epping, M.G. Willinger, C. Wolff, D. Neher, M. Antonietti, D. Dontsova, Potassium poly(heptazine imides) from aminotetrazoles: shifting band gaps of carbon nitride-like materials for more efficient solar hydrogen and oxygen evolution, *ChemCatChem* 9 (2017) 167–174.
- [28] G.G. Zhang, G.S. Li, Z.A. Lan, L.H. Lin, A. Savateev, T. Heil, S. Zafeirotas, X. C. Wang, M. Antonietti, Optimizing optical absorption, exciton dissociation, and charge transfer of a polymeric carbon nitride with ultrahigh solar hydrogen production activity, *Angew. Chem. Int. Ed.* 56 (2017) 13445–13449.
- [29] B.V. Lotsch, M. Döblinger, J. Sehnert, L. Seyfarth, J. Senker, O. Oeckler, W. Schnick, Unmasking melon by a complementary approach employing electron diffraction, solid-state nmr spectroscopy, and theoretical calculations-structural characterization of a carbon nitride polymer, *Chem. Eur. J.* 13 (2007) 4969–4980.
- [30] J.R. Holst, E.G. Gillan, From triazines to heptazines: deciphering the local structure of amorphous nitrogen-rich carbon nitride materials, *J. Am. Chem. Soc.* 130 (2008) 7373–7379.
- [31] G. Zhang, J. Zhang, M. Zhang, X. Wang, Polycondensation of thiourea into carbon nitride semiconductors as visible light photocatalysts, *J. Mater. Chem.* 22 (2012) 8083–8091.
- [32] S. Cao, J. Low, J. Yu, M. Jaroniec, Polymeric photocatalysts based on graphitic carbon nitride, *Adv. Mater.* 27 (2015) 2150–2176.
- [33] W. Ho, Z. Zhang, W. Lin, S. Huang, X. Zhang, X. Wang, Y. Huang, Copolymerization with 2,4,6-triaminopyrimidine for the rolling-up the layer structure, tunable electronic properties, and photocatalysis of g-C₃N₄, *ACS Appl. Mater. Interfaces* 7 (2015) 5497–5505.
- [34] G. Zhang, A. Savateev, Y. Zhao, L. Li, M. Antonietti, Advancing the n → π* electron transition of carbon nitride nanotubes for H₂ photosynthesis, *J. Mater. Chem. A* 5 (2017) 12723–12728.
- [35] Q. Han, C. Hu, F. Zhao, Z. Zhang, N. Chen, L. Qu, One-step preparation of iodine-doped graphitic carbon nitride nanosheets as efficient photocatalysts for visible light water splitting, *J. Mater. Chem. A* 3 (2015) 4612–4619.
- [36] H. Tang, F. Lévy, H. Berger, P.E. Schmid, Urbach tail of anatase TiO₂, *Phys. Rev. B* 52 (1995) 7771–7774.
- [37] B. Choudhury, A. Choudhury, Oxygen defect dependent variation of band gap, Urbach energy and luminescence property of anatase, anatase-rutile mixed phase and of rutile phases of TiO₂ nanoparticles, *Phys. E* 56 (2014) 364–371.
- [38] Z.H. Huang, H. Chen, L. Zhao, X. He, Y.Y. Du, W. Fang, W.X. Li, P. Tian, Constructing g-C₃N₄ quantum dots modified g-C₃N₄/GO nanosheet aerogel for UV-Vis-NIR driven highly efficient photocatalytic H₂ production, *J. Hydrog. Energ.* 44 (2019) 31041–31052.
- [39] J.Y. Qin, H.P. Zeng, Photocatalysts fabricated by depositing plasmonic Ag nanoparticles on carbon quantum dots/graphitic carbon nitride for broad spectrum photocatalytic hydrogen generation, *Appl. Catal. B-Environ.* 209 (2017) 161–173.
- [40] Q.F. Li, C. Ren, C.T. Qiu, T.C. He, Q.T. Zhang, X. Ling, Y.S. Xu, C.L. Su, Promoting near-infrared photocatalytic activity of carbon-doped carbon nitride via solid alkali activation, *Chin. Chem. Lett.* 32 (2021) 3463–3468.
- [41] Y. Guo, Q.X. Zhou, X.L. Chen, Y.Z. Fu, S.Y. Lan, M.S. Zhu, Y.K. Du, Near-infrared response Pt-tipped Au nanorods/g-C₃N₄ realizes photolysis of water to produce hydrogen, *J. Mater. Sci. Technol.* 119 (2022) 53–60.
- [42] Y.Y. Huang, Y.P. Jian, L.H. Li, D. Li, Z.Y. Fang, W.X. Dong, Y.H. Lu, B.F. Luo, R. J. Chen, Y.C. Yang, M. Chen, W.D. Shi, A NIR-responsive phytic acid nickel biomimetic complex anchored on carbon nitride for highly efficient solar hydrogen production, *Angew. Chem. Int. Ed.* 60 (2021) 5245–5249.
- [43] I. Hong, Y.A. Chen, Y.J. Hsu, K. Yong, Triple-channel charge transfer over W₁₈O₄₉/Au/g-C₃N₄ Z-scheme photocatalysts for achieving broad-spectrum solar hydrogen production, *ACS Appl. Mater. Inter.* 13 (2021) 52670–52680.
- [44] Z.H. Huang, H. Chen, X. He, W. Fang, W.X. Li, X. Du, X.H. Zeng, L. Zhao, Constructing a WC/NCN Schottky junction for rapid electron transfer and enrichment for highly efficient photocatalytic hydrogen evolution, *ACS Appl. Mater. Inter.* 13 (2021) 46598–46607.
- [45] M.S. Zhu, S. Kim, L. Mao, M. Fujitsuka, J.Y. Zhang, X.C. Wang, T. Majima, Metal-free photocatalyst for H₂ evolution in visible to near-infrared region: black phosphorus/graphitic carbon nitride, *J. Am. Chem. Soc.* 139 (2017) 13234–13242.
- [46] J. Kröger, A. Jiménez-Solano, G. Savasci, P. Rovó, I. Moudrakovski, K. Küster, H. Schlöberg, H.A. Vignolo-González, V. Duppel, L. Grunenberg, C.B. Dayan, M. Sitti, F. Podjaski, C. Ochsenfeld, B.V. Lotsch, Interfacial engineering for improved photocatalysis in a charge storing 2D carbon nitride: melamine functionalized poly(heptazine imide), *Adv. Energy Mater.* 11 (2021) 2003016.
- [47] X. Gong, O. Voznyy, A. Jain, W. Liu, R. Sabatini, Z. Piontkowski, G. Walters, G. Bappi, S. Nokhrin, O. Bushuyev, M. Yuan, R. Comin, D. McCamant, S.O. Kelley, E.H. Sargent, Electron-phonon interaction in efficient perovskite blue emitters, *Nat. Mater.* 17 (2018) 550–556.
- [48] Y. Wang, S. Guo, H. Luo, C. Zhou, H. Lin, X. Ma, Q. Hu, B. M.-h. Du, W. Ma, X. Yang, Lü, Reaching 90% photoluminescence quantum yield in one-dimensional metal halide C₄N₂H₁₄PbBr₄ by pressure-suppressed nonradiative loss, *J. Am. Chem. Soc.* 142 (2020) 16001–16006.
- [49] J. Ma, T.J. Miao, J. Tang, Charge carrier dynamics and reaction intermediates in heterogeneous photocatalysis by time-resolved spectroscopies, *Chem. Soc. Rev.* 51 (2022) 5777–5794.
- [50] X. Jiao, Z. Chen, X. Li, Y. Sun, S. Gao, W. Yan, C. Wang, Q. Zhang, Y. Lin, Y. Luo, Y. Xie, Defect-mediated electron-hole separation in one-unit-cell ZnIn₂S₄ layers for boosted solar-driven CO₂ reduction, *J. Am. Chem. Soc.* 139 (2017) 7586–7594.